A mechanistic analysis of delamination of elastic coatings from the surface of plastically deformed stents

Ó Máirtín É[1], Concannon J[1], Parry[2] G, McGarry JP[1]

[1] Biomedical Engineering, College of Engineering and Informatics, National University of Ireland Galway
2 Univ. Grenoble Alpes, CNRS, Grenoble INP, SIMAP, F-38000 Grenoble, France

Abstract

Several medical papers have reported delamination of the coating from the stent-substrate following intravascular deployment leading to adverse outcomes for patients. However, the mechanisms of delamination of such polymer coatings from the surface of a stent due to large deformations during device deployment has not been studied. In this paper, a novel and in-depth investigation of the mechanisms and parameters that govern stent-coating delamination is performed, using a cohesive zone formulation to simulation the evolution of traction at the stent-coating interface. The study firstly analyses the behaviour of elastic coatings on idealised elastic stent substrates. Simulations reveal that the mode mixity of delamination is strongly dependent on the level of stent deployment at initiation. In general, peak normal tractions exceed peak shear tractions at low levels of stent deployment whereas the reverse trend is computed at high levels of stent deployment. Interface tractions increase with both increasing stent thickness and coating thickness suggesting that thinner stents and thinner coatings should be utilised for the delivery of antiproliferative drugs in order to reduce the risk of coating delamination. Next, the influence of stent plasticity on interface tractions and coating delamination is investigated. Even at low levels of deployment, plastic yielding occurs in the stent hinge region and the patterns of normal and shear tractions are found to be significantly more complex than those computed for elastic stents, with both tensile and compressive regions of normal traction occurring in the stent arch. At a high level of stent deployment shear tractions at the stent-coating interface are computed to increase with decreasing strain hardening modulus. The findings of this paper provide a new insight into the stress-state at the stent-coating interface as a function of the stent design parameters and large deformation elasticity and plasticity during deployment, allowing for a more reliable assessment of the limits relating to safe implantation of coated stents.

Keywords: cohesive zone, stent, delamination, elastic-plastic, coating, geometric, material properties

1 Introduction

Over 20,000 published articles can be found on finite element simulations of stents. However, to the authors knowledge, fewer than ten previous papers have included stent coating delamination in finite element analysis of stent performance (two further papers include a coating in a finite element model, but simplistically assume a rigid perfect bond between the coating and stent (Lee et al., 2014; Schiavone et al., 2014)). FDA regulatory guidelines for non-clinical analysis of stent performance set a requirement for finite element analysis of stents, no guidelines or recommendations have been issued in relation to the finite element analysis of the mechanical behaviour and damage of stent coatings (FDA, 2010). The lack of mechanistic analysis of coated stents is remarkable, given that implantation of polymer coated drug eluting stents is the dominant treatment strategy for patients with symptomatic coronary artery disease (Torii et al., 2020). Moreover, the current global market value of drug eluting stents is $5.63

billion and growing. The absence of a robust body of literature on the finite element design and analysis of polymer coated stents is more surprising and alarming given that several experimental benchtop tests of drug eluting stents using scanning electron microscopy have reported delamination of polymer coatings from the stent surface during deployment (Chen et al., 2018; Fujimoto et al., 2018; Kollum et al., 2005; Levy et al., 2009). Such delamination is of critical importance from a clinical viewpoint, potentially leading to thrombosis, inflammation, micro-embolism formation and impaired drug delivery (Hoffmann et al., 2002; Kollum et al., 2005; Levy et al., 2009). Indeed, it is reasonable to suggest that delamination and fracture of coatings may result in migration of debonded fragments of drug eluting to non-diseased sections of the artery, with subsequent drug elution potentially causing significant damage to healthy arterial tissue.

The potential delamination risk of a polymer coating from a metallic stent surface should not be surprising, given that plastic strains of 30-50% develop in the hinge region of a stent during balloon expansion/deployment. Indeed the entire design principle upon which stents are based is the generation of high plastic strains so that the stent retains its expanded configuration, and thus acts as a permanent structural support to maintain a large lumen and sufficient blood flow through the previously blocked section of artery. However, only seven papers to date have presented structural analysis of coating integrity during such large plastic deformation of the metallic stent substrate (four studies by the current authors (Hopkins et al., 2016, 2013; Máirtín et al., 2014; Parry and McGarry, 2012), and three subsequent studies by Migliavacca and co-workers (Chen et al., 2018; Wu et al., 2015, 2014). These studies largely provide demonstrations of coating delamination for select number of limited commercially available coated stent designs. However, no study to date has provided a systematic analysis of the role of plastic deformation on traction distributions and delamination patterns along the stent-coating interface. The study of Parry and McGarry, (2012) presents an analytical solution for the traction distribution of an elastic coating on an elastic stent substrate. This analysis provides fundamental insight into the transition from normal tractions at the top of the stent arch region to shear tractions at the arch-strut boundary. However, the applicability of this study to the design or real stents is limited by the infinitesimal strain and linear elastic materials required for a close form analytical solution. The extension of this work to include large deformation plastic deformation of the stent substrate is an essential step to advance the current state-of-the-art of stent design. The development of a robust mechanistic approach to stent coating design is of particular importance, given the current industry goals of reducing strut thickness so that stents can be deployed in highly stenosed and calcified vessels (Lee and Hernandez, 2018), and the emerging technology of coated biodegradable polymer stents (Cassese et al., 2018; Kalra et al., 2017; Misra et al., 2017; Rebagay and Bangalore, 2019).

While mechanistic analysis of stent-coating interface tractions and delamination is largely absent from the stent literature, the study of bi-layer systems is a long-established branch of mechanics (Freund and Suresh, 2004). Such studies largely focus on coatings on flat semi-infinite substrates. For example, it is well known that compressed layers are susceptible to buckling induced delamination especially when the residual compression is large and the interface has low delamination toughness (Faou et al., 2012; Hutchinson and Suo, 1991). Finite element analyses of thermal barrier coatings have been presented by (Sait et al., 2020; Zhu et al., 2015). Chen et al., (2015) calculated the fracture energy release rate for brittle elastic coatings on ductile elasto-plastic substrates. The case of thin elastic films delaminating from cylindrical substrates has been investigated (Hutchinson, 2001), and the effect of subsequent ridge cracking has been studied (Faulhaber et al., 2006). This kind of damage occurs for thin films on very thick substrates and when very large compressive stresses are present in the film due to deposition methods, differences in thermal expansion coefficients or when the coating is an oxide scale developing on a metallic substrate. In contrast, stents are structural elements

with a film to substrate thickness ratio ranging from 0.01 to 0.5 and a small residual stress. The interface damage is rather linked to the large displacement imposed to the structure during deployment, resulting in plasticity in the substrate and heterogeneous strain distributions in both coating and substrates.

The overall aim of the study is to uncover the complex distributions of traction at the stent-coating interface due to large elastic and plastic deformation during stent deployment. The insights provided by the systematic analysis may be used to motivate further mechanistic analysis and design and regulatory guidelines for next-generation polymer coated drug-eluting stents. Firstly, in order to gain an in-depth understanding of the mechanics of coating delamination due to finite deformation stent deformation, hyperelastic coatings on hyperelastic stent substrates are simulated. Specifically, the influence of stent geometry (strut length, strut thickness and coating thickness) on interface tractions and coating delamination is analysed. Such analysis of elastic stent substrates may be relevant to next-generation biodegradable polymer stent substrates (Lee and Hernandez, 2018). The influence of stent plasticity on interface tractions and coating delamination is then investigated. We demonstrate that large plastic deformation of the stent-substrate (the very basis of balloon expandable metallic stent designs) profoundly affect the distribution of traction at the stent-coating interface. Analyses suggest that reliable design of coated stent systems cannot be performed without finite deformation computational plasticity simulation.

2 Model Construction

Parameterisation of stent geometry for finite element investigation

Stent geometries consists of a series of interconnected repeating units, as shown in **Figure 1(a)**, with each repeating unit consisting of an arch connected to straight struts (Parry & McGarry, 2012). The reference configuration of the stent and coating geometry utilised in the present study is depicted in **Figure 1(b)**. A 2D unit cell idealisation is utilised and stent and coating dimensions are chosen based on commercially available stent designs (Regar *et al.*, 2001). A di (a) ment boundary condition is applied on the bottom edge of the strut to simulate stent d(ıent. A polar coordinate system (r,θ) is utilised with the stent-coating interface located at r=R. The coating material and the stent materials are identified as layers 1 and 2, of thickness h_1 and h_2 respectively. The arch and strut sections are also clearly indicated in **Figure 1(b)** along with the strut length, L. The distance along the stent-coating interface, x, originating at the top of the arch (x⁄(R=0)) is also indicated. A custom python code was developed to automatically generate stent meshes for parametric analysis. Both stent and coating are meshed using generalised plane strain elements. A mesh sensitivity study reveals that ten elements through the thickness of the coating provides a converged solution in terms of peak interface tangential traction at $x/R = \pi/2$. Coatings are modelled as Neo-Hookean hyperelastic materials. In section 3.1 the stent material is modelled as neo-Hookean elastic materials, representative of next-generation polymer stents. In Section 3.2 the stent material is modelled using J2 plasticity materials with isotropic hardening, representative of metallic balloon expandable stents.

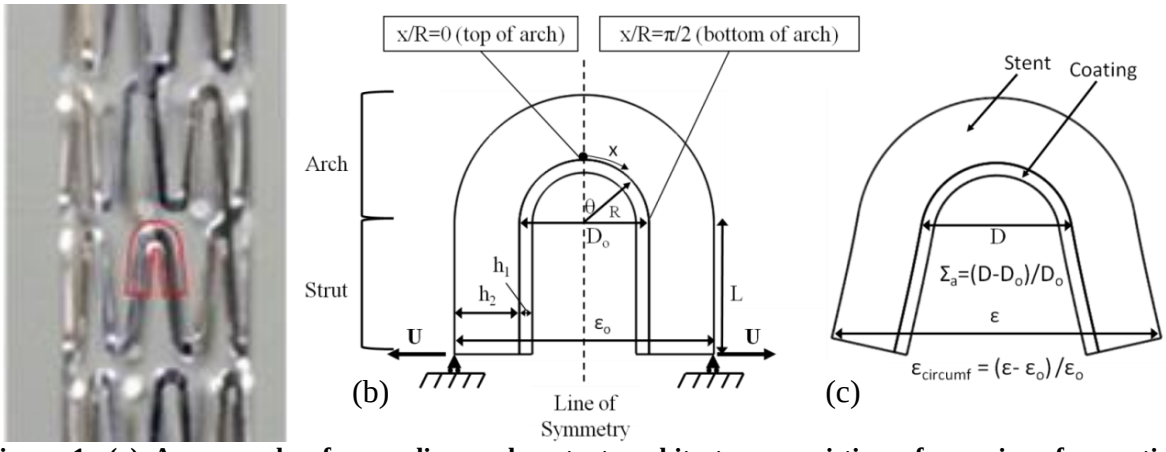

Figure 1: (a) An example of a cardiovascular stent architecture consisting of a series of repeating interconnected unit cells (highlighted), where each unit cell consists of an arch connected to straight struts (Parry and McGarry, 2012). (b) Geometry of the stent and stent coating in the initial configuration. Boundary conditions at the base of the stent struts and applied displacements, U, are highlighted at the strut ends. The radial distance to the stent-coating interface, R, and the distance along the stent-coating interface from the top of the arch, x, is also indicated. The arch and strut sections are also highlighted. The coating thickness, h_1, stent thickness, h_2 and strut length, L, are also shown. (c) Geometry of a deployed stent configuration with the stent and coating materials highlighted. The arch deployment (Σ_a) and circumferential strain ($\varepsilon_{circumf}$) are also defined, with ε_o and D_o defined in (b).

As the arch deformation is the critical determinant of the interface tractions (Parry & McGarry, 2012), non-dimensional arch deformation is defined as;

$$\Sigma_a = (D - D_0)/D_0 \tag{1.01}$$

where D_0 and D are the initial and final arch deployments respectively, as depicted in **Figure 1(b,c)**. Σ_a is referred to as the *deployment level* for the remainder of this paper.The circumferential strain $(\varepsilon_{circumf})$ is also defined in **Figure 1(c)** as;

$$\varepsilon_{circumf} = (\varepsilon - \varepsilon_0)/\varepsilon_0 \tag{1.02}$$

Cohesive Zone Formulation

The interface between the stent (substrate) and the coating is modelled using mixed mode cohesive zone formulations previously developed by(McGarry et al., 2014). Mixed mode interface separation ($\Delta_n > 0$) is modelled using the following expression for normal traction T_n and tangential traction T_t

$$T_n(\Delta_n, \Delta_t) = \sigma_{max} exp(1) \left(\frac{\Delta_n}{\delta_n}\right) exp\left(-\sqrt{\frac{\Delta_n^2}{\delta_n^2} + \frac{\Delta_t^2}{\delta_t^2}}\right) \tag{1.03}$$

$$T_t(\Delta_n, \Delta_t) = \tau_{max} exp(1) \left(\frac{\Delta_t}{\delta_t}\right) exp\left(-\sqrt{\frac{\Delta_n^2}{\delta_n^2} + \frac{\Delta_t^2}{\delta_t^2}}\right) \tag{1.04}$$

where Δ_n and Δ_t are the normal and tangential components of the interface separation vector, $\underline{\Delta}$;the normal and tangential interface characteristic lengths are δ_n and δ_t; σ_{max} is the mode I interface strength and τ_{max} is the mode II interface strength. This model provides identical behaviour in mode I and mode II separation when $\sigma_{max} = \tau_{max}$ and $\delta_n = \delta_t$. Additionally, for this specific case the traction magnitude $\sqrt{T_n^2 + T_t^2}$ is independent of the mode mixity, depending only on the separation magnitude. Furthermore, it can easily be demonstrated that

$\partial T_n/\partial \Delta_t = \partial T_t/\partial \Delta_n$, i.e. the traction separation equations can be derived from a potential function

$$\phi(\Delta_n, \Delta_t) = \phi_o + \sigma_{max} exp(1) \left(1 + \sqrt{\frac{\Delta_n^2}{\delta_n^2} + \frac{\Delta_t^2}{\delta_t^2}}\right) exp\left(-\sqrt{\frac{\Delta_n^2}{\delta_n^2} + \frac{\Delta_t^2}{\delta_t^2}}\right) \quad (1.05)$$

when $\sigma_{max} = \tau_{max}$ and $\delta_n = \delta_t$.
While equations (1.03) and (1.04) provide physically realistic coupling between normal and tangential behaviour during mixed mode separation ($\Delta_n > 0$), correctly penalization of mixed mode over-closure in the event of compressive (negative) normal interface tractions is not obtained. Therefore, when $\Delta_n < 0$ the following tractions-separation equations are implemented (McGarry *et al.*, 2014):

$$T_n(\Delta_n, \Delta_t) = \sigma_{max} \exp(1) \left(\frac{\Delta_n}{\delta_n}\right) \exp\left(-\frac{\Delta_n}{\delta_n}\right) \exp\left(-\alpha \sqrt{\frac{{\Delta_t}^2}{{\delta_t}^2}}\right) \quad (1.06)$$

$$T_t(\Delta_n, \Delta_t) = \tau_{max} \exp(1) \left(\frac{\Delta_t}{\delta_t}\right) \exp\left(-\sqrt{\frac{{\Delta_t}^2}{{\delta_t}^2}}\right) \exp\left(-\beta \frac{\Delta_n}{\delta_n}\right) \quad (1.07)$$

All symbols have the same meaning as equations (1.03) and (1.04) above, while α and β specify the weighting of the mixed mode coupling terms. Here, $\alpha = \beta = \sqrt{2} - 1$. In the current study it is assumed that $\delta_n = \delta_t = 1$ μm and $\sigma_{max} = \tau_{max}$, giving identical behaviour in mode I and mode II separation unless otherwise stated. Values of interface strength σ_{max} are selected based on the range identified in the experimental study of (Hopkins et al., 2013). The cohesive zone model is implemented in the Abaqus Standard (implicit) solver via a user-defined interface subroutine (UINTER).

3 Parametric Analysis

3.1 Elastic Stent

In this section, elastic material properties are utilised to describe both the coating and stent materials. The stent stiffness, E_s, and the coating stiffness, E_c, are chosen so that $E_s/E_c = 2.5$, unless otherwise stated. This coating to stent stiffness ratio is based on a polymer coating on a polymer stent. The choice of a relatively stiff coating is supported by the fact that diamond like carbon coatings (Kim et al., 2007) and aluminium coatings (Kollum et al., 2005) have frequently been coated on stents. In this section the influence of interface strength ($\sigma_{max}/E_c = \tau_{max}/E_c$), strut length ($L$), coating thickness ($h_1$) and stent thickness ($h_2$) on computed interface tractions is considered. Unless otherwise stated, cohesive zone parameters are chosen so that peak mode I traction and peak mode II tractions are equal ($\sigma_{max}/E_c = \tau_{max}/E_c = 2$) with the peak occurring at the same effective separation in mode I and mode II separation $\left(|T|_{max}^{\theta=0} = |T|_{max}^{\theta=\pi/2};\ |\Delta|_{max}^{\theta=0} = |\Delta|_{max}^{\theta=\pi/2}\right)$. A characteristic distance of $\delta_n = \delta_t = 0.04\mu m$ was chosen based on the parameter sensitivity and mesh sensitivity analyses. A Poisson's ratio of 0.3 is assumed for both the stent and coating materials.

Influence of Prescribed Interface Strength on the Initial Debonding Mechanism

The interface strength dramatically influences the initial delamination mechanism at the stent-coating interface. **Figure 2** shows the initial coating delamination patterns for a strut length of $L/R = 2$ when differing interaction strengths are chosen. When a low interface strength of $\sigma_{max}/E_c = \tau_{max}/E_c = 0.0019$ is prescribed (**Figure 2a(i)**), mode I coating delamination initiates at the top of the arch $(x/R = 0)$ at a moderate stent deployment $(\Sigma_a = 0.025)$. Following delamination, a significant reduction in coating stress is computed, whereas an increase in tensile stress is computed on the stent surface in the delamination region (**Figure 2a(ii)**). A markedly different pattern of coating delamination is observed if a stronger interface strength $(\sigma_{max}/E_c = \tau_{max}/E_c = 0.026)$ is prescribed. As the interface strength is high, delamination does not occur until a high level of stent deployment is reached $(\Sigma_a = 0.47)$(**Figure 2b**(i)). As demonstrated in **Figure 2b**(i), prior to the initiation of debonding $(\Sigma_a = 0.43)$ tangential tractions at the bottom of the arch become greater in magnitude than normal tractions at the top of the arch when high stent deployment levels are imposed. Again, it should be noted that this effect is particularly dominant for stents with shorter struts. Hence, predominantly mode II coating delamination initiates in the region of the bottom of the arch $(x/R = \pi/2)$. Following initiation of predominantly mode II debonding, a reduction of both tangential and normal tractions is observed at the bottom of the arch in **Figure 2b**(ii), demonstrating the importance of correct coupling in the cohesive zone formulations. The predominantly tangential separation of the interface at the bottom of the arch $(x/R = \pi/2)$ is shown in **Figure 2c**(ii). Following mode II initiation, mixed-mode delamination propagates from the bottom of the arch towards the top of the arch, as shown in **Figure 2c**(iii). The coating remains attached to the stent at the top of the arch as mode I delamination is not achieved until further deployment.

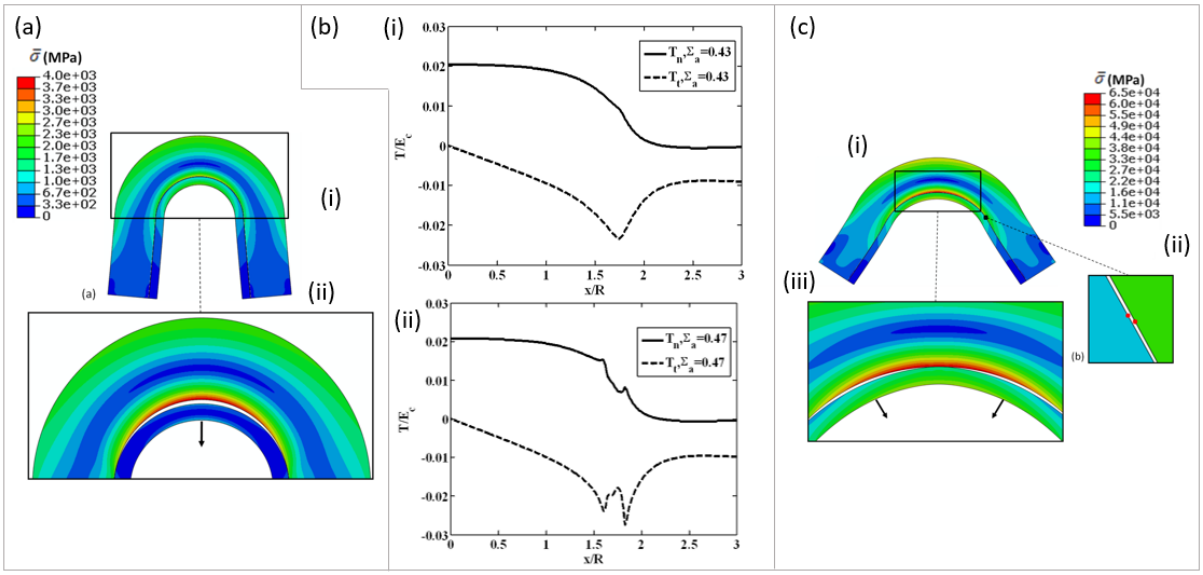

Figure 2: (a) Stent and coating von Mises stress $(\overline{\sigma})$ distribution plotted on the deformed geometry for an arch deployment, Σ_a, of (i) 0.023 and (ii) 0.025. Mode I coating delamination initiates at the top of the arch $(x/R = 0)$ as shown in (ii). $E_c = 200$GPa, $E_s = 500$GPa, $\sigma_{max}/E_c = \tau_{max}/E_c = 0.0019$, $h_1/R = 0.2$, $h_2/R = 1$, L$/R = 2$. Deformation factor =3 in (ii). (b) Computed interface traction (T/E_c) as a function of the distance along the stent-coating interface (x/R) for an arch deployment, Σ_a, of (i) 0.43 and (ii) 0.47. Predominantly mode II coating delamination initiates at the bottom of the arch $(x/R = \pi/2)$ as indicated by the reduction in traction in (ii). $E_c = 200$GPa, $E_s = 500$GPa, $\sigma_{max}/E_c = \tau_{max}/E_c = 0.026$, $h_1/R = 0.2$, $h_2/R = 1$, L$/R = 2$. (c) Stent and coating von Mises stress $(\overline{\sigma})$ distribution plotted on the deformed geometry for an arch deployment, Σ_a, of (i)-(ii) 0.47 and (iii) 0.475. Predominantly mode II coating delamination initiates at the bottom of the arch $(x/R = \pi/2)$ as shown in (ii). Mixed-mode

coating delamination computed at higher stent deployment is shown in (iii). $E_c = 200\text{GPa}$, $E_s = 500\text{GPa}$, $\sigma_{max}/E_c = \tau_{max}/E_c = 0.026$, $h_1/R = 0.2$, $h_2/R = 1$, $L/R = 2$. Deformation factor =3 for (iii).

Effect of Strut Length

In this section the effect of strut length on stent-coating interface tractions is investigated, assuming a constant stent thickness, coating thickness and stent-coating stiffness ratio for all simulations. Assuming parameters of $h_1/R = 0.2$, $h_2/R = 1$and $E_s/E_c = 2.5$, three strut length are considered:$L/R = 0.5$, $L/R = 2$, and $L/R = 10$, representing stent designs with very short, typical and very long struts respectively. **Figure 3** shows the computed normal(T_n) and tangential (T_t) tractions at the stent-coating interface for a range of strut lengths. A high interface strength is assumed for all simulations presented in **Figure 3** so that the distribution of tangential and normal tractions can be examined in the absence of interface debonding. Additionally, a high interface stiffness is assumed so that the infinitesimal strain analytical elastic solution of Parry & McGarry (2012) is reproduced when the strut is removed from the geometry. Results are presented at three stent deployment levels: Low deployment $(\Sigma_a = 0.024)$ results are shown in **Figure 3(a)**, where the solution is in the infinitesimal strain regime; Medium deployment $(\Sigma_a = 0.134)$ is shown in **Figure 3(b)**, where the solution is in the finite strain regime; High deployment $(\Sigma_a = 0.608)$ is shown in **Figure 3(c)**, again with the solution in the finite strain regime.

An examination of the computed tractions for the shortest strut length $(L/R = 0.5)$ at a low deployment $(\Sigma_a = 0.024)$ in **Figure 3(a)** reveals that the peak normal traction at the top of the arch $(x/R = 0)$ is greater than the peak tangential traction at the bottom of the arch $(x/R = \pi/2)$.A sinusoidal distribution of normal and shear traction can be observed at the interface along the arch $(0 \leq x/R \leq \pi/2)$, whereby the tangential traction reduces to 0 at the top of the arch (as required by symmetry) and the normal traction reduces to a non-zero value at the bottom of the arch $(x/R = \pi/2)$. It is worth noting that the range of tangential and normal tractions is approximately equal over the arch interface ($T_n(x/R = 0)$-$T_n(x/R = \pi/2) \approx T_t(x/R = \pi/2)$). These observations are closely aligned with the traction distribution determined by the analytical approach of Parry & McGarry (2012), where the incorporation of a strut simply effects an increased rotation of the base of the arch, reducing the tangential traction and increasing the normal traction.

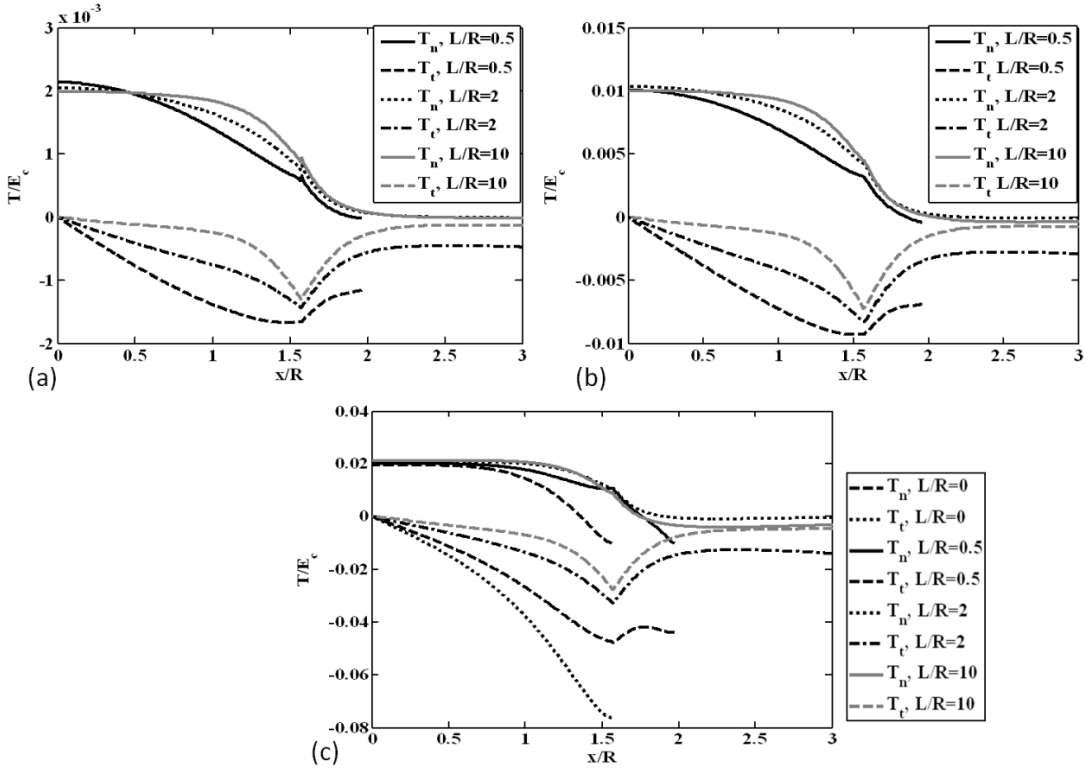

Figure 3: Computed normal $(T_n)$and tangential(T_t) tractions along the stent-coating interface for a range of strut lengths for (a) low deployment $(\Sigma_a = 0.024)$ (b) medium deployment$(\Sigma_a = 0.134)$ and (c) high deployment$(\Sigma_a = 0.608)$. At low deployment, normal tractions increase from the bottom of the arch$(x/R = \pi/2)$ to the top of the arch $(x/R = 0)$while tangential tractions increase from the top of the arch $(x/R = 0)$ to the bottom of the arch$(x/R = \pi/2)$. $E_c = 200$GPa, $E_s = 500$GPa, $\sigma_{max}/E_c = \tau_{max}/E_c = 2, h_1/R = 0.2, h_2/R = 1$.

The key observations for low deployment (infinitesimal strain) are as follows: (i) Peak normal traction occurs at the top of the arch; (ii) Peak tangential traction occurs at the bottom of the arch and is lower than the peak normal traction at the top of the arch for the range of strut lengths considered $(L/R \leq 10)$; (iii) Sinusoidal distributions are computed in the arch only for a very short strut length $(L/R \leq 0.5)$; (iv) Tractions in the strut are lower than those in the arch, with normal tractions reducing to zero and tangential tractions reducing to a constant non-zero value that depends on strut length. The patterns of computed traction for a medium deployment level ($(\Sigma_a = 0.134)$, **Figure 3(b)**) are reasonably similar to those presented for a low deployment level. However, for the highest deployment level$(\Sigma_a = 0.608)$, **Figure 3(c)**) significantly different trends can be observed. The peak tangential traction at the bottom of the arch is greater in magnitude than the peak normal traction for all strut lengths. Shorter struts lead to the greatest increase in tangential traction. Additionally, a further increase in tangential traction (and reduction in normal traction) is computed when the strut is omitted $(L/R = 0)$. The normal traction is constant for all points on the interface where $x/R < 0.5$ for all strut lengths. Additionally, it can be observed that compressive normal tractions are computed along the strut, highlighting the importance of the cohesive zone behaviour under conditions of mixed-mode over-closure.

It should be noted that for each specified value of Σ_a, the radial expansion of the stent will depend also on the strut length. This is clearly evident from **Figure 4** where stress distributions and deformed geometries for the three deployment levels $(\Sigma_a = 0.024,\ 0.134,\ 0.608)$ are shown for a strut length of $L/R = 2$ in **Figure 4(a-c)** and for a strut length of $L/R = 10$ in **Figure 4(d-f)**. For example, for the high deployment level $(\Sigma_a = 0.608)$ a strut length of $L/R = 2$ provides an 87% increase in stent radius, representing a moderate radial expansion

(as shown in **Figure 4(c)**) whereas a strut length of $L/R = 10$ provides a 466% increase in stent radius, representing a significant radial overexpansion (as shown in **Figure 4(f)**). Finally, it should be noted that rotational constraints are not imposed on the strut ends for all simulations presented in this paper, as this is representative of the majority of commercially available stent designs (McGarry *et al.*, 2004; Hopkins *et al.*, 2010). However, certain stent designs may result in a rotational constraint at the bottom of the struts, e.g. a repeating diamond arrangement of struts. This constraint essentially results in a significant increase in tangential traction for all deployment levels and also results in a normal compression at the stent–coating interface at the bottom of the arch.

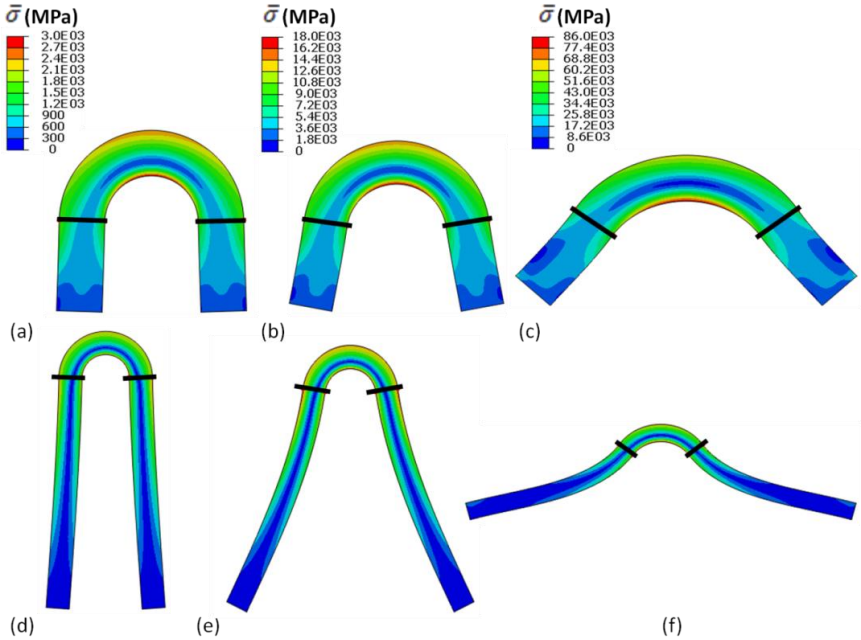

Figure 4: von Mises stress($\bar{\sigma}$)distribution for deformed stent geometries at low ($\boldsymbol{\Sigma_a = 0.024}$), medium($\boldsymbol{\Sigma_a = 0.134}$)and high($\boldsymbol{\Sigma_a = 0.608}$) deployment for (a)-(c) $\boldsymbol{L/R = 2}$ and (d)-(f)$\boldsymbol{L/R = 10}$. The black line at base of the arch is included to highlight the increase in arch rotation with increasing stent deployment.

Effect of Coating Thickness

In this section the effect of coating thickness on stent-coating interface tractions is investigated, assuming a constant stent thickness, strut length and stent-coating stiffness ratio for all simulations. **Figure 5** shows the computed normal (T_n) and tangential(T_t) tractions at the stent-coating interface for a range of coating thicknesses. Again, normal and tangential tractions are assessed in the absence of interface debonding. Interface tractions increase with coating thickness with higher normal and tangential interface tractions being computed for thicker coating at all stent deployment levels. This suggests that the use of a thinner coating could prevent coating debonding. At a low level of stent deployment ($\Sigma_a = 0.0063$) (**Figure 5 (a)**), the peak normal traction at the top of the arch ($x/R = 0$) is greater than the peak tangential traction at the bottom of the arch ($x/R = \pi/2$) for the thicker coatings ($h_1/R = 0.2; h_1/R = 0.5$). However, the peak tangential traction at the bottom of the arch is similar in magnitude to the peak normal traction at the top of the arch for the thinner coating ($h_1/R = 0.05$) with $|T/E_c| \approx 1.25\,x10^{-4}$.At medium stent deployment ($\Sigma_a = 0.236$)(**Figure 5(b)**), the peak normal traction computed at the top of the arch ($x/R = 0$) again exceeds the peak tangential traction at the bottom of the arch ($x/R = \pi/2$) except for the case of the thinner coating($h_1/R = 0.05$), where the computed peak tangential tractions are marginally greater. At high stent deployment($\Sigma_a = 0.737$)(**Figure 5(c)**), the peak tangential traction computed at the bottom of the arch exceeds the peak normal traction at the top of the

arch for all coating thicknesses. At this level of stent deployment, instead of normal traction reducing monotonically from the top of the arch towards the bottom of the arch along the arch interface ($0 \leq \mathrm{x/R} \leq \pi/2$), as seen in **Figure 5**, an increase in normal traction is computed along the interface from the top of the arch ($\mathrm{x/R} = 0$) to $\mathrm{x/R} = 1.05$ and $\mathrm{x/R} = 0.82$ for coating thicknesses of $h_1/R = 0.05, \text{and } 0.2$ respectively. A marginal increase in normal traction is also computed for the thickest coating ($h_1/R = 0.5$) from the top of the arch ($\mathrm{x/R} = 0$) to $\mathrm{x/R} = 0.28$ before reducing towards the bottom of the arch. Therefore, at a high level of stent deployment, the location of maximum normal traction is computed further from the top of the arch as coating thickness reduces. Additionally, tangential traction along the strut also increases with coating thickness.

A small degree of coating compression is computed for coating thicknesses of $h_1/R = 0.05$ and $h_1/R = 0.2$ at a low level of stent deployment (**Figure 5(a)**) along the stent strut ($x/R > \pi/2$) with no compression computed for the thickest coating. Minor coating compression is computed along the stent strut for all coating thicknesses at medium stent deployment (**Figure 5(b)**). At a high level of deployment, in the case of the thinnest coating ($h_1/R = 0.05$), maximum normal compression ($T/E_c \approx -4.8\,E - 4$) is computed in the region of the bottom of the arch at $x/R = 1.9$. Maximum normal compression is computed further along the stent strut, at $x/R = 2.2$ and 2.5 for the thicker coatings of $h_1/R = 0.2$ and 0.5 respectively. Again, it is worth noting that the cohesive zone formulation correctly penalises mixed-mode coating over-closure along the stent struts.

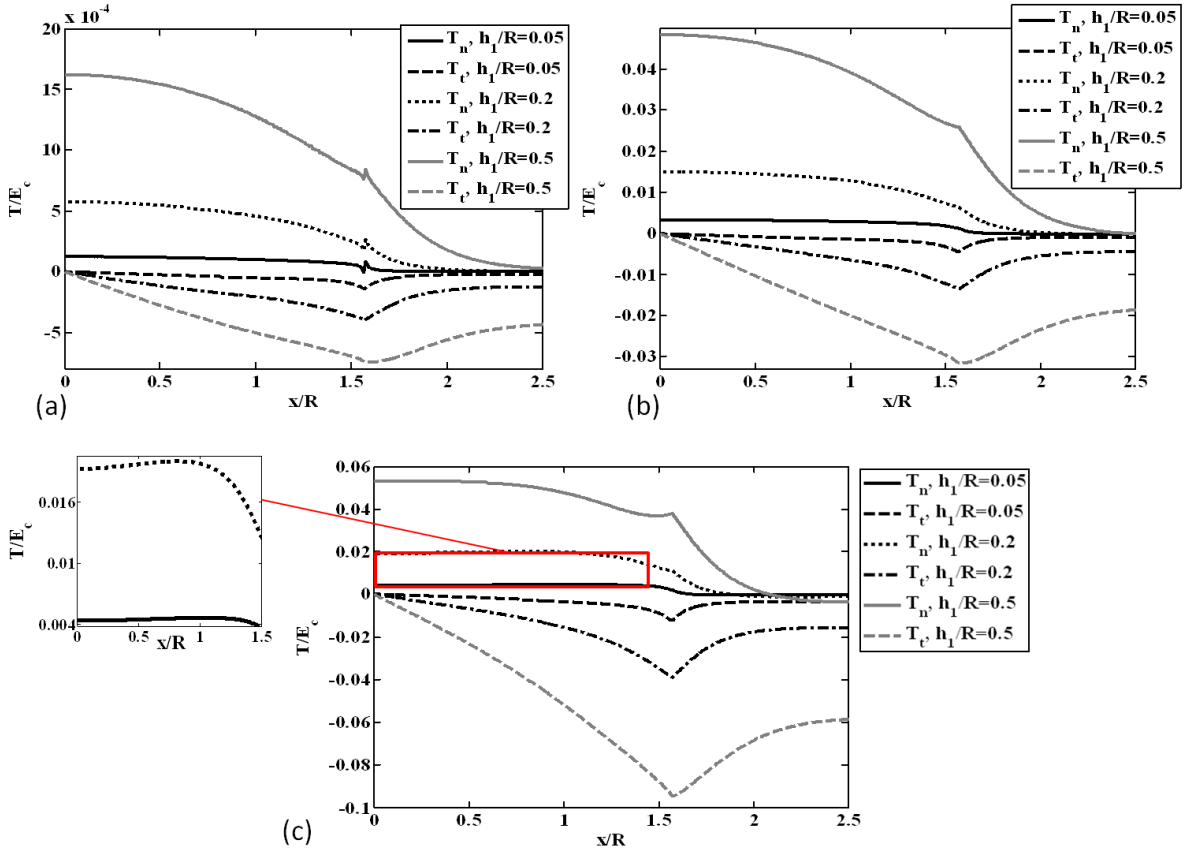

Figure 5: Computed normal $(T_n)$and tangential(T_t) tractions along the stent-coating interface for a range of coating thicknesses for (a) low deployment $(\Sigma_a = 0.0063)$ (b) medium deployment$(\Sigma_a = 0.236)$ and (c) high deployment$(\Sigma_a = 0.737)$. The insert in (c) shows increasing normal tractions away from the top of the arch $(x/R = 0)$ for $h_1/R = 0.05$ and 0.2. $E_c = 200$GPa, $E_s = 500$GPa, $\sigma_{max}/E_c = \tau_{max}/E_c = 2$, $h_2/R = 1$, $\mathrm{L}/R = 2$.

Effect of Stent Thickness

In this section the effect of stent thickness on stent-coating interface tractions is investigated, assuming a constant coating thickness, strut length and stent-coating stiffness ratio for all simulations. Analyses presented in previous sections assume a stent thickness of $h_2/R = 1$, based on typical dimensions of commercially available stents. In **Figure 6**, three additional stent thicknesses are considered: $h_2/R = 5$ (significantly thicker than typical commercially available stent designs); $h_2/R = 0.5$ (significantly thinner than typical commercially available stent designs; $h_2/R = 0.1$ (unconventionally thin stent: In this case, the coating is twice as thick as the stent). The investigation of stent thickness on stent-coating interface traction is particularly relevant given recent clinical studies that suggest that thinner stent struts lead to reduced rates of restenosis (Kastrati et al., 2001; Turco et al., 2008). **Figure 6** shows the computed normal (T_n) and tangential (T_t) tractions at the stent-coating interface for the three aforementioned stent thicknesses. At a low level of stent deployment $(\Sigma_a = 0.017)$ (**Figure 6(a)**) interface tractions generally increase with stent thickness. However, a 10-fold increase in stent thickness from $h_2/R = 0.5$ to $h_2/R = 5$ results in only a ~2 fold increase in peak normal traction at the top of the arch. Peak normal tractions at the top of the arch $(x/R = 0)$ are greater than the peak tangential tractions at the bottom of the arch $(x/R = \pi/2)$ for all stent thicknesses. Most notably, tangential tractions are negligible for the thinnest stent geometry $(h_2/R = 0.1)$ at a low level of deployment. Similar trends can also be observed at a medium level of stent deployment $(\Sigma_a = 0.327)$, as shown in **Figure 6(b)**.

In contrast to lower stent deployment (**Figure 6(a)** and **(b)**), at a high level of stent deployment $(\Sigma_a = 0.831)$ (**Figure 6(c)**) peak tangential tractions are greater than peak normal tractions for all strut thicknesses, in particular for thinner struts $(h_2/R = 0.1, 0.5)$. Normal (T_n/E_c) and tangential (T_t/E_c) tractions are depicted in two separate figures in part (c) to enhance the visualisation of the tractions. Interestingly, for the two thinnest stents, the normal tractions decrease from the values computed for the lower deployment level considered in **Figure 6(b)**. In fact, negligible normal tractions are computed for the thinnest stent design $(h_2/R = 0.1)$. Additionally, coating compression is computed in the region of maximum tangential traction (the bottom of the arch) for the thinnest stent. Tangential tractions are significantly higher than normal tractions at the high deployment level for all stent thicknesses. From a design perspective, very thin stent struts will result in dominant normal tractions at low deployment levels, and dominant tangential tractions at high deployment levels.

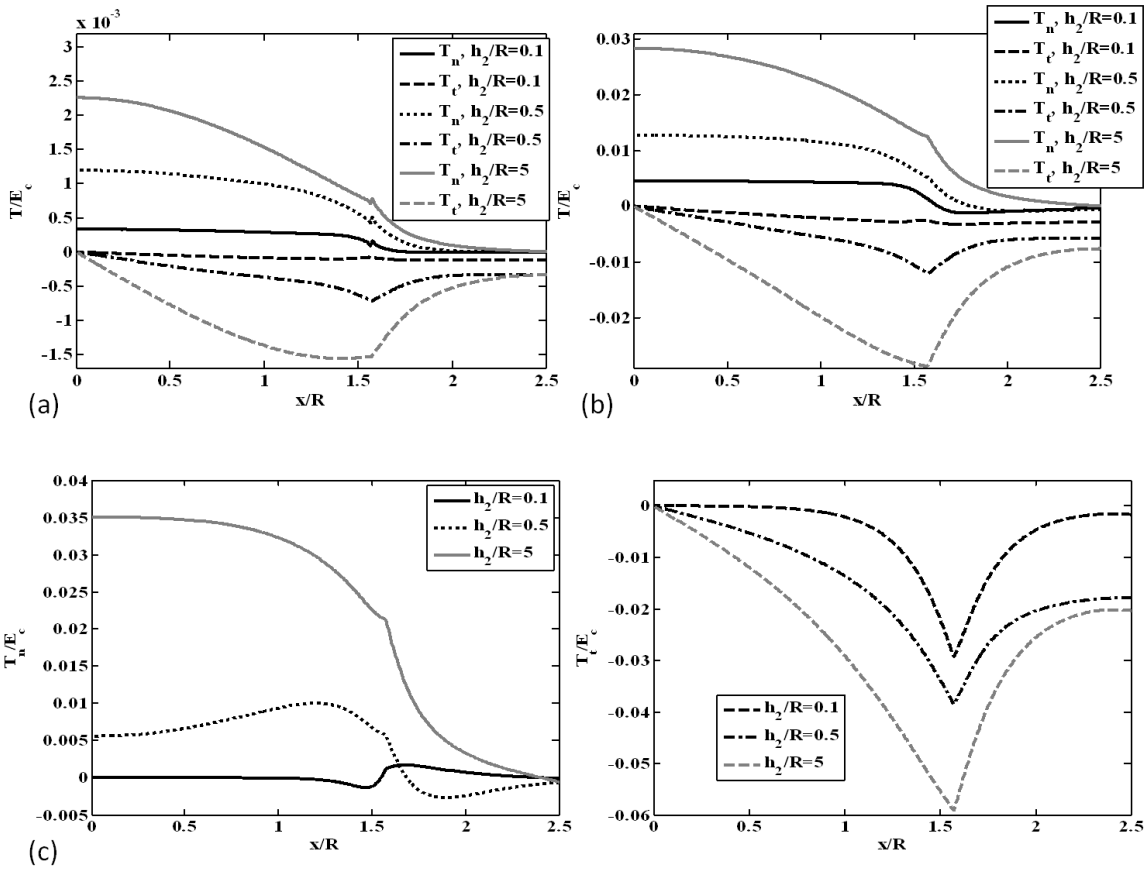

Figure 6: Computed normal $(T_n)$and tangential(T_t) tractions along the stent-coating interface for a range of strut thicknesses for (a) low deployment $(\Sigma_a = 0.017)$ (b) medium deployment $(\Sigma_a = 0.327)$ and (c) high deployment $(\Sigma_a = 0.831)$. Computed normal (T_n/E_c) and tangential (T_t/E_c) tractions are shown separately in (c) to enhance the visualisation. $E_c = 200$GPa, $E_s = 500$GPa, $\sigma_{max}/E_c = \tau_{max}/E_c = 2$, $h_1/R = 0.2$, L$/R = 2$.

Further results on the influence of (i) stent-coating stiffness ratio, (ii) Mode I to Mode II interface strength ratio on coating delamination, and (iii) geometrical parameters on peak tangential to peak normal interface traction ratio can be found in the Supplementary Material Sections (A-C) respectively.

3.2 Elastic-Plastic Stent

In this section, the influence of stent plasticity on computed interface tractions is investigated. Plastic deformation is required for the correct functionality of a metallic balloon expandable stent. Plastic strains of 30-50% are developed in the region of the arch while the diameter of the stent increases by a factor of 3-5 during balloon deployment (McGarry *et al.*, 2004). Typically, elastic recoil results in a 2-5% reduction in deployed diameter following balloon removal.

Analysis of Interface Tractions Without Coating Debonding

A high interface strength is assumed for all simulations presented in this section so that the distribution of tangential and normal tractions can be examined in the absence of interface debonding.In this section, computed interface tractions are presented for a range of both yield stresses $(\sigma_y = 80\text{MPa}, 200\text{ MPa and } 600\text{ MPa})$ and stent strain hardening moduli $(E_h = 2\text{MPa}, 20\text{ MPa and } 200\text{ MPa})$. Coatings are modelled as elastic materials with a Young's modulus $(E_c = 20\text{MPa})$, based on the stiffness range of commercially available polymer coatings(Yung & Cooper, 1998; Antony *et al.*, 2003). In all cases, coating thickness $(h_1/R = 0.2)$ and strut length $(\text{L}/R = 2)$ are based on the reference stent geometry. A

Young's modulus (E_s) of 200GPa, yield stress (σ_y) of 200MPa and Poisson's ratio (ν) of 0.3 is chosen for the elastic-plastic stent material (representative of 316L stainless steel) unless otherwise stated.

Influence of Yield Stress

Figure 7 reveals the influence of yield stress on the computed normal(T_n) and tangential (T_t) tractions at the stent-coating interface. It is shown that yield stress (σ_y) dramatically influences the computed interface tractions, particularly at high levels of stent deployment. Three yield stresses are considered, $\sigma_y = 80$MPa, 200MPa, and 600MPa, representative of the yield stress of biodegradable magnesium, 316L stainless steel, and cobalt chromium, respectively. At a low level of stent deployment ($\Sigma_a = 0.056$), peak tangential traction exceeds peak normal traction for each yield stress considered (**Figure 7(a)**). Even at this low deployment level, yielding occurs in all three cases and the patterns of normal and tangential tractions differ significantly to those reported for elastic stents in previous sections of this paper. Peak tangential tractions are computed close to the top of the arch at $x/R = 0.4$ with greatest tangential traction computed for $\sigma_y = 200MPa$. A minimum in normal traction is computed in all cases at $x/R = 0.36$ with coating compression (characterised by negative normal traction) computed for $\sigma_y = 200MPa$. In all cases two local maxima are computed for normal traction, one at the top of the arch ($x/R = 0$) and one at $x/R \approx 0.6$.

At a medium level of stent deployment ($\Sigma_a = 0.303$), the largest normal and tangential tractions are computed at the top of the arch ($x/R = 0$) and at $x/R = 0.375$ respectively for $\sigma_y = 600MPa$ (**Figure 7(b)**). Furthermore, significant coating compression is computed for $\sigma_y = 600MPa$, from $0.26 \leq x/R \leq 0.43$. In the case of the lower yield stresses ($\sigma_y = 80MPa$ and $200MPa$) the peak normal traction is not computed at the top of the arch and does not fluctuate very significantly along the arch interface. Yield stress has a significant influence on the location and magnitude of maximum tangential traction at this deployment level with peak tangential traction computed at $x/R = 0.85$ and $x/R = 0.57$ for $\sigma_y = 80MPa$ and $200MPa$ respectively. At a high stent deployment ($\Sigma_a = 0.627$) similar trends in tangential traction are computed (**Figure 7(c)**). Significant coating compression is again computed for $\sigma_y = 600\ MPa$ from $0.16 \leq x/R \leq 0.47$. Interestingly, relative to **Figure 7(b)**, a significant decrease in normal traction is computed at the top of the arch ($x/R = 0$), for $\sigma_y = 200\ MPa$, with negligible normal traction computed($T/E_s \sim 1.7x10^{-6}$). Similar to **Figure 7(b)**, largest normal and tangential tractions traction are still computed for $\sigma_y = 600\ MPa$ at the top of the arch ($x/R = 0$)and at $x/R = 0.37$ respectively.

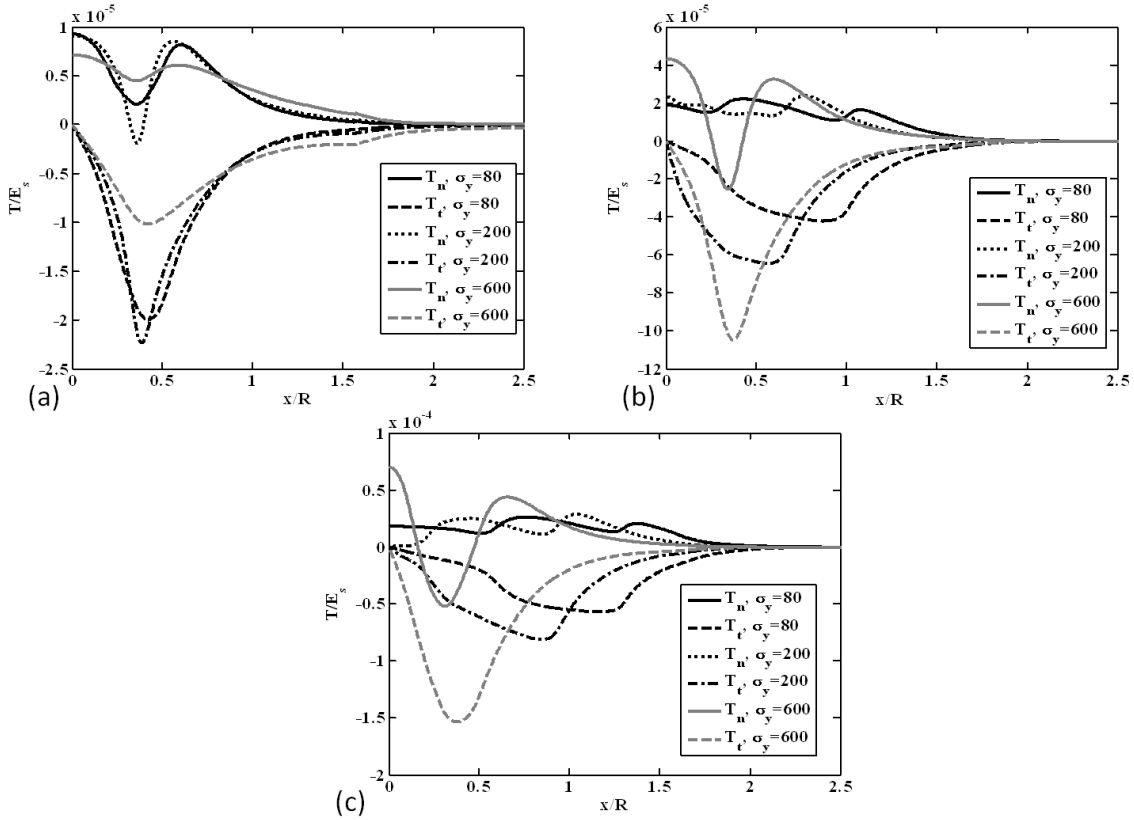

Figure 7: Computed normal (T_n) and tangential (T_t) tractions along the stent-coating interface for a range of yield stresses $(\sigma_y = 80MPa, 200MPa, 600MPa)$, for (a) low deployment$(\Sigma_a = 0.056)$ (b) medium deployment $(\Sigma_a = 0.303)$ and (c) high deployment $(\Sigma_a = 0.627)$. In all cases, an elastic coating$(E_c = 200MPa)$ is considered. For the elastic-plastic stent, $E_s = 200GPa$, the strain hardening modulus, $E_h =$ 20MPa, and yield stress. $L/R = 2$, $h_1/R = 0.2$, $h_2/R = 1$. $\sigma_{max}/E_s = \tau_{max}/E_s = 2$.

Influence of Stent Strain Hardening on Interface Tractions

The computed normal(T_n) and tangential(T_t) tractions for a range of stent strain hardening moduli $(E_h = 2$MPa, 20 MPa and $200MPa)$are shown in **Figure 8** for a coating stiffness (E_c) of $200MPa$. At a low stent deployment, the influence of stent strain hardening modulus on interface traction distributions is not significant (**Figure 8(a)**). At medium stent deployment $(\Sigma_a = 0.255)$, it is evident that the strain hardening modulus significantly affects the computed traction distributions (**Figure 8(b)**).The greatest normal and tangential tractions are computed for $E_h = 2MPa$ at this level of stent deployment. For $E_h = 2MPa$ and $20MPa$, peak tangential tractions are computed in the same location along the stent-coating interface as minimum normal tractions at $x/R \approx 0.4$. At a high level of stent deployment $(\Sigma_a = 0.5)$, the greatest normal and tangential tractions are again computed for $E_h = 2MPa$ (**Figure 8(c)**). However, it should be noted that the location of peak normal traction is computed at $x/R \approx 0.9$ while a significant reduction in normal traction is computed at the top of the arch for $E_h = 2MPa$ and $20MPa$. This reduction in normal traction can be attributed to the high concentration of plastic deformation in the region of the top of the arch at high stent deployment. Lowest tangential tractions are computed for the stiffer strain hardening modulus $(E_h = 200MPa)$ for $x/R < 0.7$.

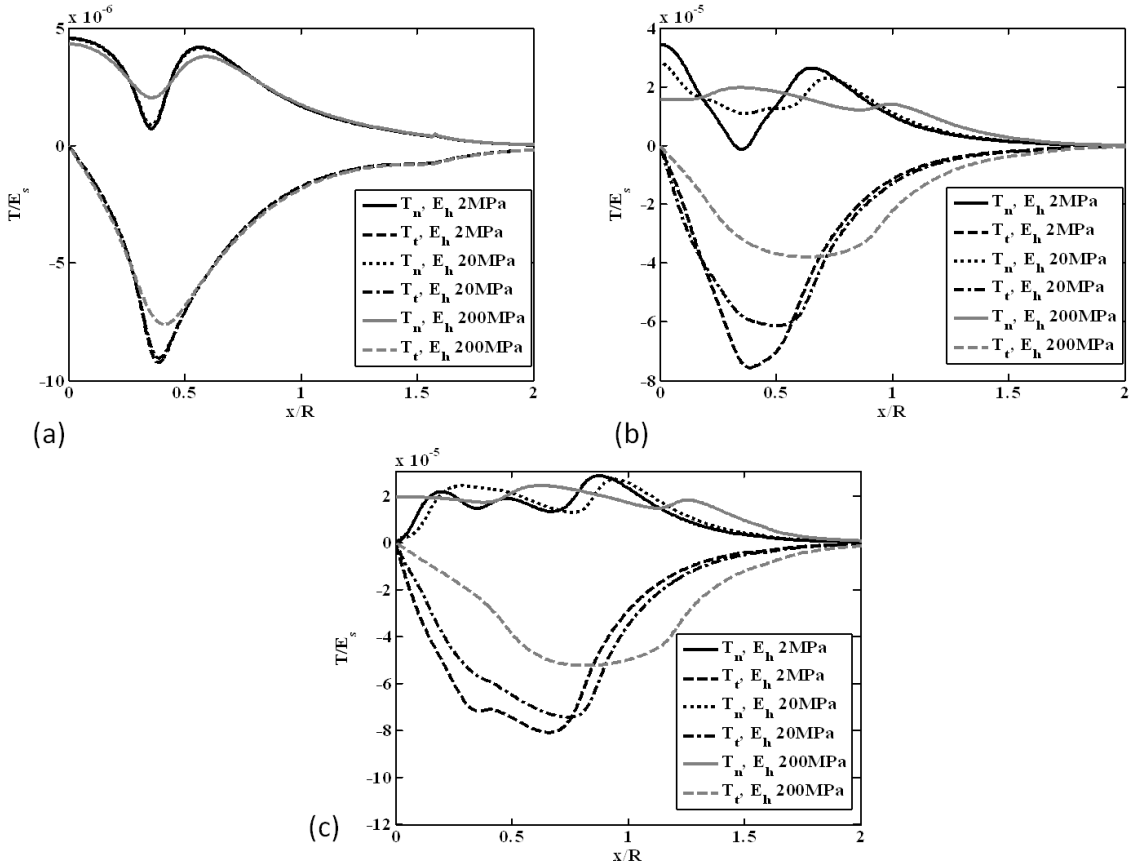

Figure 8: Computed normal (T_n) and tangential (T_t) tractions along the stent-coating interface for (a) low deployment$(\Sigma_a = 0.03)$ (b) medium deployment$(\Sigma_a = 0.255)$ and (c) high deployment$(\Sigma_a = 0.5)$ for an elastic-plastic stent with the substrate thickness, $h_2/R = 1$. Three strain hardening moduli are considered for the strut $(E_h = 2, 20 \text{ and } 200MPa)$. In all cases, an elastic coating$(E_c = 200MPa)$ is considered.$h_1/R = 0.2, E_s = 200GPa$, $L/R = 2$, $\sigma_{max}/E_s = \tau_{max}/E_s = 2$. The strut yield stress $(\sigma_y) = 200MPa$.

Analysis of Coating Debonding Mechanisms

The previous section illustrates that complex distributions of normal and tangential traction are computed along the stent-coating interface when plastic deformation of the stent is considered. The ratio of normal to tangential traction at any point on the interface is shown to be highly dependent on the deployment level in addition to the yield stress and strain hardening modulus. While delamination is not considered in the previously presented analyses of plastically deforming stents, with a very strong stiff interface being assumed, the complex traction distributions suggest that if a lower interface strength is considered the location and mode mixity of debonding will be highly dependent on several factors, including deployment level at debonding initiation, ratio of normal to tangential interface strength, in addition to stent geometric and material parameters. In the final section of this paper, two examples of diverse coating debonding patterns during deployment of a plastically deforming stent are presented. The first example entails debonding of a coating from a thin stent geometry $(h_2/R = 0.1)$ and the second example entails the debonding of a coating from a thick stent geometry $(h_2/R = 2)$. These debonding simulations do not represent an exhaustive collection of all possible debonding patterns. They merely serve to illustrate some possible debonding patterns that emerge as a result of the complex distributions of normal and tangential tractions at the stent–coating interface in the case of a plastically deforming stent.

Coating Debonding Behaviour for a Thin Stent Strut Design $(\boldsymbol{h_2/R = 0.1})$

For the thin stent geometry $(h_2/R = 0.1)$ it can be seen that tangential tractions are dominant at an arch deployment of $\Sigma_a = 0.371$ for $E_c = 20MPa$ and $E_h = 200MPa$ with peak tangential tractions computed at $x/R = 0.75$. In the first sample simulation of coating debonding, presented in **Figure 9**, interface strengths are chosen so that coating debonding initiates at this level of deployment. Furthermore, it is assumed that mode I and mode II interface strengths are equal$(\sigma_{max}/E_s = \tau_{max}/E_s = 2\text{x}10^{-6})$. The coating node located at $x/R = 0.75$ is highlighted in **Figure 9(b)**. Corresponding interface tractions are depicted in **Figure 9(c)** and **(d)**. Mixed-mode delamination is initially computed at the interface at $x/R = 0.75$as shown in **Figure 9(b)**. As stent deployment increases, a predominantly mode II delamination is computed at the interface with $T_t/\tau_{max} \approx 0.914$ (**Figure 9(c)**). Due to the dominant mode II type delamination, the resistance to normal separation is significantly reduced with computed peak normal traction of $T_n/\sigma_{max} \approx 0.46$ (**Figure 9(d)**). No coating compression is computed at the stent-coating interface. Following full coating delamination at $x/R = 0.75$, mixed-mode delamination progresses along the interface with pure mode I coating delamination eventually occurring at the top of the arch $(x/R = 0)$. Further progression of coating delamination at higher stent deployment is shown in **Figure 9(e)**. However, at the level of stent deployment shown in **Figure 9(e)**, pure mode I delamination has not yet occurred.

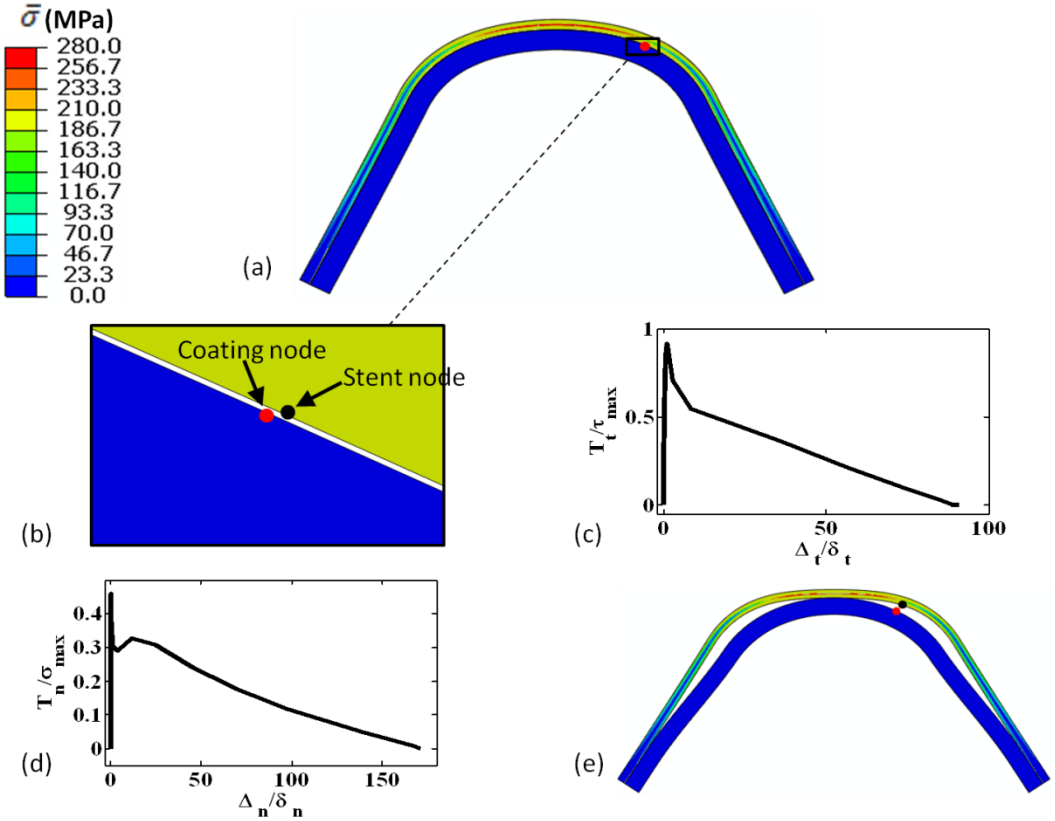

Figure 9: (a) Stent and coating von Mises $(\bar{\sigma})$ stress distribution plotted on the deformed geometry at an arch deployment of $\Sigma_a = 0.371$ (b) Mixed-mode coating delamination computed at $x/R = 0.75$ (c) Normalised tangential traction (T_t/τ_{max}) as a function of normalised tangential separation (Δ_t/δ_t) computed at coating node $(x/R = 0.75)$. (d) Normalised normal traction (T_n/σ_{max}) as a function of normalised normal separation (Δ_n/δ_n) computed at coating node $(x/R = 0.75)$. (e) von Mises $(\bar{\sigma})$ stress distribution plotted on the deformed stent geometry at an arch deployment of $\Sigma_a = 0.42$. An elastic coating$(E_c = 20MPa)$ is considered. Elastic-plastic properties are assigned for the stent strut with $E_s = 200GPa$, strain hardening modulus, $E_h = 200MPa$ and yield stress, $\sigma_y = 200MPa$. $h_1/R = 0.2, h_2/R = 0.1, L/R = 2$, $\sigma_{max}/E_s = \tau_{max}/E_s = 2x10^{-6}$.

Coating Debonding Behaviour for a Thick Stent Strut Design $(\boldsymbol{h_2/R = 2})$

In the final sample simulation of coating debonding from a plastically deforming stent a thick stent geometry $(h_2/R = 2)$ is considered, with $E_c = 200MPa\,, E_h = 2MPa$. The interface strengths are reduced so that debonding initiates at a deployment level of $\Sigma_a = 0.101$, assuming that the normal and tangential interface strengths are equal ($\sigma_{max}/E_s = \tau_{max}/E_s = 4.8\,\text{x}10^{-5}$). The peak tangential traction is computed at $x/R \approx 0.6$ at this low level of deployment as indicated by the non-debonding simulation shown in Supplementary Material **Figure S10**. Additionally, in this region the coating is compressed normally into the stent surface, hence nodes in this region undergo mixed-mode over-closure. The node at $x/R = 0.6$ is highlighted in **Figure 10(a)**. The insert shown in **Figure 10(b)** illustrates the mixed-mode over-closure of the node. It can be noted that while the coating is compressed into the stent surface, the magnitude of over-closure is very small, as the cohesive zone framework penalises such mixed-mode over-closure (characterised by the computation of a rapid increase in negative normal tractions highlighted by red arrow in **Figure 10(e)**). During the debonding of the node highlighted in **Figure 10**, the compression of the node into the stent surface is reversed and the node separates from the stent in a mixed-mode fashion. Resistance to normal separation is significantly reduced due to the earlier initiation of tangential debonding, with peak normal traction of $T_n/\sigma_{max} \approx 0.17$ being computed (**Figure 10(e)**). The insert in **Figure 10(d)** illustrates the final mixed-mode separation of the node from the stent surface. Further progression of coating delamination at higher stent deployment is shown in **Figure 10(f)** where coating delamination is computed all along the arch, including pure mode I debonding at the top of the arch $(x/R = 0)$. The insert in **Figure 10(f)** shows that the stent surface at the interface becomes highly non-uniform at finite deformation. Such non-uniform undulations on the surface of a plastically deforming stent surface underlie the complex patterns of interface traction and mixed-mode delamination illustrated in this study.

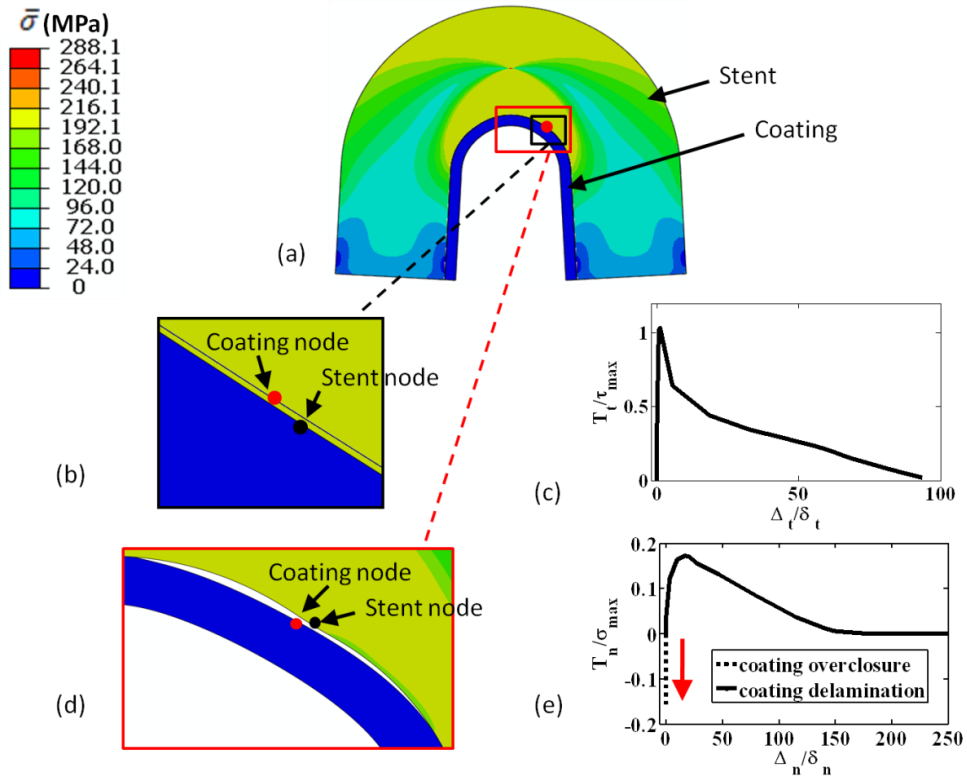

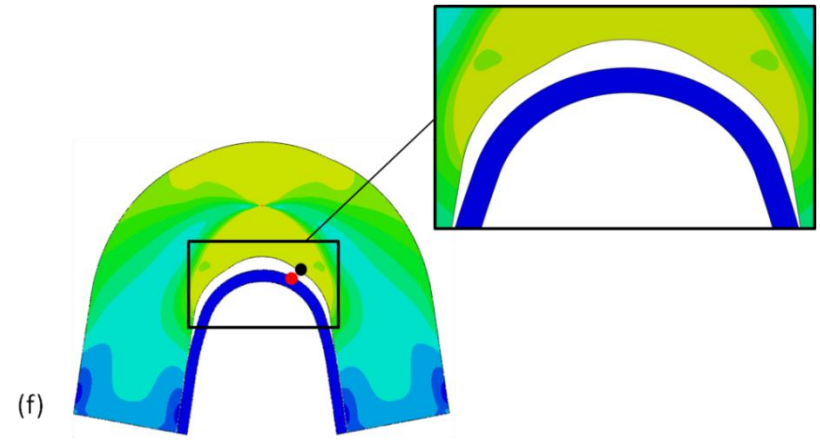

Figure 10: (a) Stent and coating von Mises ($\overline{\sigma}$) stress distribution plotted on the deformed geometry at an arch deployment of $\Sigma_a = 0.098$ (b) Mixed-mode coating compression computed at $x/R = 0.6$ (c) Normalised tangential traction (T_t/τ_{max}) as a function of normalised tangential separation (Δ_t/δ_t) computed at coating node ($x/R = 0.6$) (d) Mixed-mode coating delamination computed at $x/R = 0.6$ and $\Sigma_a = 0.112$ (e) Normalised normal traction (T_n/σ_{max}) as a function of normalised normal separation (Δ_n/δ_n) computed at coating node ($x/R = 0.6$). (f) von Mises ($\overline{\sigma}$) stress distribution plotted on the deformed stent geometry at an arch deployment, $\Sigma_a = 0.305$. Insert highlights non-uniform strut surface. An elastic coating($E_c = 200MPa$) is considered. Elastic-plastic properties are assigned for thestent strut with $E_s = 200GPa$, strain hardening modulus, $E_h = 2MPa$ and yield stress, $\sigma_y = 200MPa$. $h_1/R = 0.2, L/R = 2, h_2/R = 2$. $\sigma_{max}/E_c = \tau_{max}/E_c = 4.8 \text{ x} 10^{-5}$. Deformation factor=3 for (b) and (d).

Corresponding results for thin (h_2/R=0.1) and thick (h_2/R=2) stent struts are presented in the Supplementary Material Sections (D) and (E) respectively.

4 Concluding Remarks

Several medical papers have reported delamination of the coating from the stent-substrate following intravascular deployment leading to adverse outcomes for patients. However, the mechanisms of delamination of such polymer coatings from the surface of a stent due to large deformations during device deployment had not been investigated before. In this paper, a novel and in-depth investigation of the mechanisms and parameters that govern stent-coating delamination is performed, using a cohesive zone formulation to simulate the evolution of traction at the stent-coating interface. The study firstly analyses the behaviour of elastic coatings on idealised elastic stent substrates. Such analysis of elastic stent substrates may be relevant to next-generation biodegradable polymer stent substrates (Lee and Hernandez, 2018). Simulations reveal that the mode mixity of delamination is strongly dependent on the level of stent deployment at initiation. In general, peak normal tractions exceed peak shear tractions at low levels of stent deployment whereas the reverse trend is computed at high levels of stent deployment. Interface tractions increase with both increasing stent thickness and coating thickness suggesting that thinner stents and thinner coatings should be utilised for the delivery of antiproliferative drugs in order to reduce the risk of coating delamination. Next, the influence of stent plasticity on interface tractions and coating delamination is investigated. Even at low levels of deployment, plastic yielding occurs in the stent hinge region and the patterns of normal and shear tractions are found to be significantly more complex than those computed for elastic stents, with both tensile and compressive regions of normal traction occurring in the stent arch. At a high level of stent deployment shear tractions at the stent-coating interface are computed to increase with decreasing strain hardening modulus. This study represents a significant advancement on the study of Hopkins *et al.* (2010) where interface traction distributions were not examined and only mode I debonding initiation at the top of the arch was considered. This study also represents a significant advance on analytical solution for stent-coating interface tractions for infinitesimal linear elastic deformation developed by Parry & McGarry (2012).

The findings of this paper provide a new insight into the stress-state at the stent-coating interface as a function of the stent design parameters and plastic deformation during deployment, allowing for a more reliable assessment of the limits relating to safe implantation of coated stents.

In this study the influence of geometrical parameters (strut length and stent thickness) and material properties (yield stress and strain hardening modulus) on the stress state at a stent-coating interface is investigated. The influence of finite deformation on interface tractions is examined, significantly advancing on the analytical analyses of Parry & McGarry (2012) which were limited to infinitesimal linear elastic deformations. Most importantly, the present paper also considers the effect of stent plasticity on interface tractions and provides simulations of coating debonding.

The current study demonstrates that the mechanisms of coating debonding are complex and depend on numerous stent, coating and interface design criteria. The full complexity of coating debonding for elastic and elastic-plastic stents is uncovered. Several experimental studies using scanning electron microscopy have reported extensive delamination of polymer coatings from the stent surface during deployment (Basalus and von Birgelen, 2010; Levy et al., 2009; Otsuka et al., 2007; Wiemer et al., 2010). Numerous studies have suggested that coating damage may play a significant role in late stent thrombosis, following the use of drug-eluting stents (Balakrishnan et al., 2005; Daemen et al., 2007; Hoffmann et al., 2002; Iakovou et al., 2005; Levy et al., 2009; Lüscher et al., 2007; Otsuka et al., 2007; Wang et al., 2002). It is reasonable to suggest that some of the other clinical implications associated with coating damage may include micro-embolism formation, impaired drug delivery and obstruction of blood flow. Therefore, computational analyses and reliable design techniques are required in order to determine the limits relating to the safe implantation of coated stents. The analyses presented in this paper provide valuable insight into the stress-state at the stent-coating interface as a function of the stent design parameters. Such analyses allow for a more reliable assessment of the limits relating to safe implantation of coated stents.

Future extensions of this work should include simulation of the stent microstructure using crystal plasticity formulations (Liu et al., 2018; McGarry et al., 2007; Shanthraj et al., 2015) and strain gradient plasticity (Gurtin, 2008; Qu et al., 2006). Future implementations should consider nitinol shape memory alloy stent substrates (Arghavani et al., 2010; Grabe and Bruhns, 2009; Sedlák et al., 2012). Simulations should also consider coating/stent due to cyclic loading due to cardiac motion and blood pressure (Han et al., 2020; McCarthy et al., 2014a, 2014b). Non-linear hyper-viscoelastic behaviour should be considered for simulation of commercially used drug eluting polymers. Interaction between stent coatings and the occluded artery wall should also be simulated, including endothelial cell denudation due to interaction with stent coatings (Reynolds et al., 2014; McGarry and McHugh, 2008). Analysis should also investigate the fracture of thin struts during deployment due to webbing coating defects (Hopkins et al., 2016). Experimental characterisation should be performed to determine the stent-coating interface mode I, mode II and mixed mode fracture strength. The coating strength implemented in the simulation of debonding from a thin strut stent design ($\sigma_{max}/E_s = 2\text{x}10^{-6}$) is similar to that measured by Hopkins et al., (2013) for a polyurethane Chronoflex coating bonded to a stainless steel substrate ($\sigma_{max}/E_s = \sim 1.5\text{x}10^{-6}$. However, the analyses above suggest that such an interface strength is insufficient for stent struts within the range of thicknesses used commercially.

Key implications for the improved design of coated stents uncovered in this study are summarised below.

An **elastic stent** is first considered in order to develop an initial fundamental understanding of interface traction behaviour. A number of important findings are revealed for an elastic stent:

- Firstly, it is important to note that peak normal tractions exceed peak tangential tractions at low stent deployment whereas peak tangential tractions exceed peak normal tractions at high stent deployment (finite deformation) when interface tractions are assessed for a range of strut lengths, stent thicknesses and coating thicknesses. Since stents typically undergo high deployment levels, mode II coating debonding initiation at the bottom of the arch should be carefully considered.
- The implementation of a longer stent strut effects an increased rotation at the base of the stent arch which reduces the tangential tractions and increases the normal tractions along the stent-coating interface. This effect can be counteracted by using a shorter strut design.
- It is shown that interface tractions increase with coating thickness suggesting that antiproliferative drugs should be delivered via a thinner coating in order to reduce the risk of coating debonding. Commercially available stent coatings range in thickness from $10-20\mu m$ (Hopkins et al., 2010). Since interface tractions increase with increasing coating thickness, a higher bond strength must be achieved when thicker coatings are utilised.
- The influence of stent thickness on interface tractions is particularly relevant given that clinical studies suggest that thinner stent struts lead to reduced rates of restenosis (Kastrati et al., 2001; Turco et al., 2008). Interface tractions increase with increasing stent thickness suggesting that thinner stents should be utilised to reduce the risk of coating delamination. Increased tangential tractions and negligible normal tractions are computed for a thin stent at high stent deployment due to excessive straightening of the thin stent geometry.

In the second section of this study, an **elastic-plastic stent** is considered:

- Yield stress is shown to significantly influence the location and magnitude of peak normal and tangential interface tractions. Additionally, a high yield stress$\left(\sigma_y = 600\ MPa\right)$is shown to promote significant coating compression at high deployment.
- Interface tractions are also presented for a range of stent strain hardening moduli. For a typical stent thickness $(h_2/h_1 = 5)$, the strain hardening modulushas a significant influence on the computed interface tractions at high stent deployment.
- For a thin elastic-plastic stent $(h_2/h_1 = 0.5)$, it is demonstrated that the prescribed ratio of peak tangential to peak normal traction significantly alters the mechanism and location of initial coating debonding. A highly non-uniform stent surface is computed at the stent-coating interface for a thick elastic-plastic stent. In this case, mixed-mode coating over-closure is computed prior to mixed-mode coating delamination, highlighting the importance of implementing a cohesive zone formulation which can appropriately penalise mixed-mode compression.

5 Acknowledgements

Funding: The authors acknowledge funding from Science Foundation Ireland grant no. 18/ERCD/5481

6 Author Contributions

E. O'M: Formal analysis; Methodology; Writing
JC: Writing; Formal analysis
GP: Conceptualization; Formal analysis; Methodology; Software
PMcG: Conceptualization; Formal analysis; Methodology; Writing; Software; Supervision

7 References

Antony, P., Puskas, J.E., Kontopoulou, M., 2003. Investigation of the Rheological and Mechanical Properties of a Polystyrene-Polyisobutylene-Polystyrene Triblock Copolymer and Its Blends With Polystyrene. Polym. Eng. Sci. 43, 243–253. https://doi.org/10.1002/pen.10021

Arghavani, J., Auricchio, F., Naghdabadi, R., Reali, A., Sohrabpour, S., 2010. A 3-D phenomenological constitutive model for shape memory alloys under multiaxial loadings. Int. J. Plast. 26, 976–991. https://doi.org/10.1016/j.ijplas.2009.12.003

Balakrishnan, B., Tzafriri, A.R., Seifert, P., Groothuis, A., Rogers, C., Edelman, B.R., 2005. Strut position, blood flow, and drug deposition: Implications for single and overlapping drug-eluting stents. Circulation 111, 2958–2965. https://doi.org/10.1161/CIRCULATIONAHA.104.512475

Basalus, M., von Birgelen, C., 2010. Benchside testing of drug-eluting stent surface and geometry. Interv. Cardiol. 2.

Cassese, S., Xhepa, E., Ndrepepa, G., Kufner, S., Colleran, R., Giacoppo, D., Koppara, T., Mankerious, N., Byrne, R.A., Laugwitz, K.-L., Schunkert, H., Fusaro, M., Kastrati, A., Joner, M., 2018. Vascular response to percutaneous coronary intervention with biodegradable-polymer vs. new-generation durable-polymer drug-eluting stents: a meta-analysis of optical coherence tomography imaging trials. Eur. Hear. Journal-Cardiovascular Imaging 19, 1294–1301. https://doi.org/10.1093/ehjci/jex334

Chen, C., Tan, J., Wu, W., Petrini, L., Zhang, L., Shi, Y., Cattarinuzzi, E., Pei, J., Huang, H., Ding, W., Yuan, G., Migliavacca, F., 2018. Modeling and Experimental Studies of Coating Delamination of Biodegradable Magnesium Alloy Cardiovascular Stents. ACS Biomater. Sci. Eng. 4, 3864–3873. https://doi.org/10.1021/acsbiomaterials.8b00700

Chen, F.L., He, X., Prieto-Muñoz, P.A., Yin, H.M., 2015. Opening-mode fractures of a brittle coating bonded to an elasto-plastic substrate. Int. J. Plast. 67, 171–191. https://doi.org/10.1016/j.ijplas.2014.10.007

Daemen, J., Wenaweser, P., Tsuchida, K., Abrecht, L., Vaina, S., Morger, C., Kukreja, N., Jüni, P., Sianos, G., Hellige, G., van Domburg, R.T., Hess, O.M., Boersma, E., Meier, B., Windecker, S., Serruys, P.W., 2007. Early and late coronary stent thrombosis of sirolimus-eluting and paclitaxel-eluting stents in routine clinical practice: data from a large two-institutional cohort study. Lancet 369, 667–678. https://doi.org/10.1016/S0140-6736(07)60314-6

Delannay, L., Jacques, P.J., Kalidindi, S.R., 2006. Finite element modeling of crystal plasticity with grains shaped as truncated octahedrons. Int. J. Plast. 22, 1879–1898. https://doi.org/10.1016/j.ijplas.2006.01.008

Faou, J.Y., Parry, G., Grachev, S., Barthel, E., 2012. How does adhesion induce the formation of telephone cord buckles? Phys. Rev. Lett. 108, 116102. https://doi.org/10.1103/PhysRevLett.108.116102

Faulhaber, S., Mercer, C., Moon, M.-W., Hutchinson, J.W., Evans, A.G., 2006. Buckling delamination in compressed multilayers on curved substrates with accompanying ridge cracks. J. Mech. Phys. Solids 54, 1004–1028. https://doi.org/10.1016/j.jmps.2005.11.005

FDA, 2010. Non-Clinical Engineering Tests and Recommended Labeling for Intravascular Stents and Associated Delivery Systems [WWW Document].

Freund, L.B., Suresh, S., 2004. Thin Film Materials, Thin Film Materials. Cambridge University Press. https://doi.org/10.1017/cbo9780511754715

Fujimoto, Y., Kobayashi, Y., Kato, K., Yamaguchi, M., 2018. Delamination of novel ultrathin bioabsorbable abluminal polymer of platinum chromium everolimus-eluting stent. Cardiovasc. Interv. Ther. 33, 97–98. https://doi.org/10.1007/s12928-016-0442-9

Grabe, C., Bruhns, O.T., 2009. Path dependence and multiaxial behavior of a polycrystalline

NiTi alloy within the pseudoelastic and pseudoplastic temperature regimes. Int. J. Plast. 25, 513–545. https://doi.org/10.1016/j.ijplas.2008.03.002

Gurtin, M.E., 2008. A finite-deformation, gradient theory of single-crystal plasticity with free energy dependent on densities of geometrically necessary dislocations. Int. J. Plast. 24, 702–725. https://doi.org/10.1016/j.ijplas.2007.07.014

Han, S., Yang, X., Shi, D., Miao, G., Huang, J., Li, R., 2020. Microstructure-sensitive modeling of competing failure mode between surface and internal nucleation in high cycle fatigue. Int. J. Plast. 126, 102622. https://doi.org/10.1016/j.ijplas.2019.11.001

Hoffmann, R., Mintz, G.S., Haager, P.K., Bozoglu, T., Grube, E., Gross, M., Beythien, C., Mudra, H., vom Dahl, J., Hanrath, P., 2002. Relation of stent design and stent surface material to subsequent in-stent intimal hyperplasia in coronary arteries determined by intravascular ultrasound. Am. J. Cardiol. 89, 1360–4. https://doi.org/10.1016/s0002-9149(02)02347-0

Hopkins, C., McHugh, P.E., O'Dowd, N.P., Rochev, Y., McGarry, J.P., 2013. A combined computational and experimental methodology to determine the adhesion properties of stent polymer coatings. Comput. Mater. Sci. 80, 104–112. https://doi.org/10.1016/j.commatsci.2013.03.029

Hopkins, C., Sweeney, C.A., O'Connor, C., McHugh, P.E., McGarry, J.P., 2016. Webbing and Delamination of Drug Eluting Stent Coatings. Ann. Biomed. Eng. 44, 419–431. https://doi.org/10.1007/s10439-015-1490-5

Hopkins, C.G., McHugh, P.E., McGarry, J.P., 2010. Computational investigation of the delamination of polymer coatings during stent deployment. Ann. Biomed. Eng. 38, 2263–2273. https://doi.org/10.1007/s10439-010-9972-y

Hutchinson, J.W., 2001. Delamination of compressed ÿlms on curved substrates, Journal of the Mechanics and Physics of Solids.

Hutchinson, J.W., Suo, Z., 1991. Mixed Mode Cracking in Layered Materials. Adv. Appl. Mech. 29, 63–191. https://doi.org/10.1016/S0065-2156(08)70164-9

Iakovou, I., Schmidt, T., Bonizzoni, E., Ge, L., Sangiorgi, G.M., Stankovic, G., Airoldi, F., Chieffo, A., Montorfano, M., Carlino, M., Michev, I., Corvaja, N., Briguori, C., Gerckens, U., Grube, E., Colombo, A., 2005. Incidence, predictors and outcome of thrombosis after succesful implantation of drug-eluting stents. J. Am. Med. Assoc. 293, 2126–2130. https://doi.org/10.1001/jama.293.17.2126

Kalra, A., Rehman, H., Khera, S., Thyagarajan, B., Deepak, &, Bhatt, L., Kleiman, N.S., Yeh, R.W., 2017. New-Generation Coronary Stents: Current Data and Future Directions. https://doi.org/10.1007/s11883-017-0654-1

Kan, Q., Kang, G., 2010. Constitutive model for uniaxial transformation ratchetting of super-elastic NiTi shape memory alloy at room temperature. Int. J. Plast. 26, 441–465. https://doi.org/10.1016/j.ijplas.2009.08.005

Kastrati, A., Mehilli, J., Dirschinger, J., Dotzer, F., Schühlen, H., Neumann, F.J., Fleckenstein, M., Pfafferott, C., Seyfarth, M., Schömig, A., 2001. Intracoronary stenting and angiographic results: Strut thickness effect on restenosis outcome (ISAR-STEREO) trial. Circulation 103, 2816–2821. https://doi.org/10.1161/01.CIR.103.23.2816

Kim, H.J., Moon, M.W., Kim, D.I., Lee, K.R., Oh, K.H., 2007. Observation of the failure mechanism for diamond-like carbon film on stainless steel under tensile loading. Scr. Mater. 57, 1016–1019. https://doi.org/10.1016/j.scriptamat.2007.07.042

Kollum, M., Farb, A., Schreiber, R., Terfera, K., Arab, A., Geist, A., Haberstroh, J., Wnendt, S., Virmani, R., Hehrlein, C., 2005. Particle debris from a nanoporous stent coating obscures potential antiproliferative effects of tacrolimus-eluting stents in a porcine model of restenosis. Catheter. Cardiovasc. Interv. https://doi.org/10.1002/ccd.20213

Lagoudas, D., Hartl, D., Chemisky, Y., MacHado, L., Popov, P., 2012. Constitutive model for

the numerical analysis of phase transformation in polycrystalline shape memory alloys. Int. J. Plast. 32–33, 155–183. https://doi.org/10.1016/j.ijplas.2011.10.009
Lee, D.H., Hernandez, J.M. d. la T., 2018. The newest generation of drug-eluting stents and beyond. Eur. Cardiol. Rev. 13, 54–59. https://doi.org/10.15420/ecr.2018:8:2
Lee, S., Lee, C.W., Kim, C.S., 2014. FEA study on the stress distributions in the polymer coatings of cardiovascular drug-eluting stent medical devices. Ann. Biomed. Eng. 42, 1952–1965. https://doi.org/10.1007/s10439-014-1047-z
Levy, Y., Mandler, D., Weinberger, J., Domb, A.J., 2009. Evaluation of drug-eluting stents' coating durability - Clinical and regulatory implications. J. Biomed. Mater. Res. - Part B Appl. Biomater. 91, 441–451. https://doi.org/10.1002/jbm.b.31420
Liu, C., Shanthraj, P., Diehl, M., Roters, F., Dong, S., Dong, J., Ding, W., Raabe, D., 2018. An integrated crystal plasticity-phase field model for spatially resolved twin nucleation, propagation, and growth in hexagonal materials. Int. J. Plast. 106, 203–227. https://doi.org/10.1016/j.ijplas.2018.03.009
Lüscher, T.F., Joner, M., Virmani, R., Eberli, F.R., Tanner, F.C., Nakazawa, G., Steffel, J., 2007. Drug-Eluting Stent and Coronary Thrombosis. Circulation 115, 1051–1058. https://doi.org/10.1161/circulationaha.106.675934
Máirtín, É.Ó., Parry, G., Beltz, G.E., McGarry, J.P., 2014. Potential-based and non-potential-based cohesive zone formulations under mixed-mode separation and over-closure-Part II: Finite element applications. J. Mech. Phys. Solids 63, 363–385. https://doi.org/10.1016/j.jmps.2013.08.019
McCarthy, O.J., McGarry, J.P., Leen, S.B., 2014a. The effect of grain orientation on fretting fatigue plasticity and life prediction. Tribol. Int. 76, 100–115. https://doi.org/10.1016/j.triboint.2013.09.023
McCarthy, O.J., McGarry, J.P., Leen, S.B., 2014b. Micro-mechanical modelling of fretting fatigue crack initiation and wear in Ti-6Al-4V. Int. J. Fatigue 62, 180–193. https://doi.org/10.1016/j.ijfatigue.2013.04.019
McGarry, J.P., McHugh, P.E., 2008. Modelling of in vitro chondrocyte detachment. J. Mech. Phys. Solids 56, 1554–1565. https://doi.org/10.1016/j.jmps.2007.08.001
McGarry, J.P., O'Donnell, B.P., McHugh, P.E., McGarry, J.G., 2004. Analysis of the mechanical performance of a cardiovascular stent design based on micromechanical modelling. Comput. Mater. Sci. 31, 421–438. https://doi.org/10.1016/j.commatsci.2004.05.001
McGarry, J.P., O'Donnell, B.P., McHugh, P.E., O'Cearbhaill, E., McMeeking, R.M., 2007. Computational examination of the effect of material lnhomogeneity on the necking of stent struts under tensile loading. J. Appl. Mech. Trans. ASME 74, 978–989. https://doi.org/10.1115/1.2722776
McGarry, J.P., Ó Máirtín, É., Parry, G., Beltz, G.E., 2014. Potential-based and non-potential-based cohesive zone formulations under mixed-mode separation and over-closure. Part I: Theoretical analysis. J. Mech. Phys. Solids 63, 336–362. https://doi.org/10.1016/j.jmps.2013.08.020
Meissonnier, F.T., Busso, E.P., O'Dowd, N.P., 2001. Finite element implementation of a generalised non-local rate-dependent crystallographic formulation for finite strains, in: International Journal of Plasticity. Pergamon, pp. 601–640. https://doi.org/10.1016/S0749-6419(00)00064-4
Misra, S.K., Ostadhossein, F., Babu, R., Kus, J., Tankasala, D., Sutrisno, A., Walsh, K.A., Bromfield, C.R., Pan, D., 2017. 3D-Printed Multidrug-Eluting Stent from Graphene-Nanoplatelet-Doped Biodegradable Polymer Composite. Adv. Healthc. Mater. 6, 1700008. https://doi.org/10.1002/adhm.201700008
Nakane, K., Ohno, N., Tsuda, M., Yagi, Y., Nakagawa, I., Atsumi, T., 2008. Thermal ratcheting

of solder-bonded elastic and elastoplastic layers. Int. J. Plast. 24, 1819–1836. https://doi.org/10.1016/j.ijplas.2007.12.008

Otsuka, Y., Chronos, N.A.F., Apkarian, R.P., Robinson, K.A., 2007. Scanning electron microscopic analysis of defects in polymer coatings of three commercially available stents: comparison of BiodivYsio, Taxus and Cypher stents. J. Invasive Cardiol. 19, 71–6.

Parry, G., McGarry, P., 2012. An analytical solution for the stress state at stent-coating interfaces. J. Mech. Behav. Biomed. Mater. 10, 183–196. https://doi.org/10.1016/j.jmbbm.2012.02.009

Qu, S., Huang, Y., Pharr, G.M., Hwang, K.C., 2006. The indentation size effect in the spherical indentation of iridium: A study via the conventional theory of mechanism-based strain gradient plasticity. Int. J. Plast. 22, 1265–1286. https://doi.org/10.1016/j.ijplas.2005.07.008

Rebagay, G., Bangalore, S., 2019. Biodegradable Polymers and Stents: the Next Generation? Curr. Cardiovasc. Risk Rep. https://doi.org/10.1007/s12170-019-0617-x

Regar, E., Sianos, G., Serruys, P., 2001. Stent development and local drug delivery. Br. Med. Bull. 59, 227–248.

Reynolds, N.H., Ronan, W., Dowling, E.P., Owens, P., McMeeking, R.M., McGarry, J.P., 2014. On the role of the actin cytoskeleton and nucleus in the biomechanical response of spread cells. Biomaterials 35, 4015–4025. https://doi.org/10.1016/j.biomaterials.2014.01.056

Sait, F., Gurses, E., Aslan, O., 2020. Modeling and simulation of coupled phase transformation and stress evolution in thermal barrier coatings. Int. J. Plast. 102790. https://doi.org/10.1016/j.ijplas.2020.102790

Schiavone, A., Zhao, L.G., Abdel-Wahab, A.A., 2014. Effects of material, coating, design and plaque composition on stent deployment inside a stenotic artery - Finite element simulation. Mater. Sci. Eng. C 42, 479–488. https://doi.org/10.1016/j.msec.2014.05.057

Sedlák, P., Frost, M., Benešová, B., Ben Zineb, T., Šittner, P., 2012. Thermomechanical model for NiTi-based shape memory alloys including R-phase and material anisotropy under multi-axial loadings. Int. J. Plast. 39, 132–151. https://doi.org/10.1016/j.ijplas.2012.06.008

Shanthraj, P., Eisenlohr, P., Diehl, M., Roters, F., 2015. Numerically robust spectral methods for crystal plasticity simulations of heterogeneous materials. Int. J. Plast. 66, 31–45. https://doi.org/10.1016/j.ijplas.2014.02.006

Torii, S., Jinnouchi, H., Sakamoto, A., Kutyna, M., Cornelissen, A., Kuntz, S., Guo, L., Mori, H., Harari, E., Paek, K.H., Fernandez, R., Chahal, D., Romero, M.E., Kolodgie, F.D., Gupta, A., Virmani, R., Finn, A. V., 2020. Drug-eluting coronary stents: insights from preclinical and pathology studies. Nat. Rev. Cardiol. https://doi.org/10.1038/s41569-019-0234-x

Turco, M.A., Ormiston, J.A., Popma, J.J., Hall, J.J., Mann, T., Cannon, L.A., Webster, M.W.I., Mishkel, G.J., O'Shaughnessy, C.D., McGarry, T.F., Mandinov, L., Dawkins, K.D., Baim, D.S., 2008. Reduced Risk of Restenosis in Small Vessels and Reduced Risk of Myocardial Infarction in Long Lesions With the New Thin-Strut TAXUS Liberté Stent. 1-Year Results From the TAXUS ATLAS Program. JACC Cardiovasc. Interv. 1, 699–709. https://doi.org/10.1016/j.jcin.2008.09.007

Wang, F., Stouffer, G.A., Waxman, S., Uretsky, B.F., 2002. Late coronary stent thrombosis: Early vs. late stent thrombosis in the stent era. Catheter. Cardiovasc. Interv. 55, 142–147. https://doi.org/10.1002/ccd.10041

Wiemer, M., Butz, T., Schmidt, W., Schmitz, K.P., Horstkotte, D., Langer, C., 2010. Scanning electron microscopic analysis of different drug eluting stents after failed implantation:

From nearly undamaged to major damaged polymers. Catheter. Cardiovasc. Interv. 75, 905–911. https://doi.org/10.1002/ccd.22347

Wu, W., Mercuri, M., Pedroni, C., Migliavacca, F., Petrini, L., 2015. A computational study to investigate debonding in coated bioresorbable stents, in: Journal of Mechanics in Medicine and Biology. World Scientific Publishing Co. Pte Ltd, p. 1540015. https://doi.org/10.1142/S0219519415400151

Wu, W., Petrini, L., Altomare, L., Farè, S., Tremamunno, R., Yu, Z., Migliavacca, F., 2014. Modeling and experimental studies of peeling of polymer coating for biodegradable magnesium alloy stents. Xiyou Jinshu Cailiao Yu Gongcheng/Rare Met. Mater. Eng. 43, 2877–2882. https://doi.org/10.1016/s1875-5372(15)60025-x

Yung, L.Y.L., Cooper, S.L., 1998. Neutrophil adhesion on phosphorylcholine-containing polyurethanes. Biomaterials 19, 31–40. https://doi.org/10.1016/S0142-9612(97)00220-2

Zhang, M., Zhang, J., McDowell, D.L., 2007. Microstructure-based crystal plasticity modeling of cyclic deformation of Ti-6Al-4V. Int. J. Plast. 23, 1328–1348. https://doi.org/10.1016/j.ijplas.2006.11.009

Zhu, W., Yang, L., Guo, J.W., Zhou, Y.C., Lu, C., 2015. Determination of interfacial adhesion energies of thermal barrier coatings by compression test combined with a cohesive zone finite element model. Int. J. Plast. 64, 76–87. https://doi.org/10.1016/j.ijplas.2014.08.003